

Time-series estimation using transition networks on realistic, sparse flow data

Giovanni Iacobello,^{1,*} Frieder Kaiser,^{1,†} and David E. Rival¹

¹*Department of Mechanical and Materials Engineering,
Queen's University, Kingston, Ontario, K7L 3N6, Canada*

(Dated: July 9, 2021)

Inspired by biological swimming and flying that utilizes distributed haptic sensors to control complex flows, we propose a data-driven approach for load estimation relying on complex networks. We exploit sparse, real-time pressure inputs combined with pre-trained transition networks to estimate aerodynamic loads in unsteady and highly-separated flows. The transition networks contain the aerodynamic states of the system as nodes along with the underlying dynamics as links. Two network strategies are proposed and tested on realistic experimental data from the flow around an accelerating elliptical plate at various angles of attack. Aerodynamic loads are then estimated for angles of attack cases not included in the training dataset to simulate the estimation process. Performance and limitations of the two network strategies are discussed, showing that transition networks can represent a versatile data-driven alternative for real-time signal estimation using sparse and noisy signals in realistic flows.

I. INTRODUCTION

The instantaneous loads in swimming and flying in nature are highly sensitive to environmental perturbations, such as the wakes of other animals or gusts in the atmosphere, respectively. Despite challenging boundary conditions, animals control the flow over their propulsors (i.e., wings or flippers) with ease and even utilize unsteady flows to their advantage [1, 2]. Biological sensory systems monitor the flow in real-time (see FIG.1a,b) by gathering haptic feedback at multiple locations on the propulsors. By combining the sensor input with their experience, animals instantaneously estimate and control their present aerodynamic state (e.g., the aerodynamic loads) [3, 4]. These insights have inspired a series of studies adapting the multi-sensor principle for the control of autonomous aerial vehicles. In the absence of simple aerodynamic models for three-dimensional (3D) and highly-separated flows, data-driven methods have been proposed that utilize sparse pressure data to characterize the instantaneous aerodynamic state on an arbitrary body (e.g., a wing) under a variety of conditions. Examples include attached flow, separated two-dimensional flows, weakly-separated, and highly-separated three-dimensional flows [5–8].

Data-driven methods have been shown to be a valid option for load estimation, but they usually tend to perform well only within a limited range of unsteady boundary conditions. Large training datasets are usually required, and very sparse pressure distributions represent a big challenge for data-driven methods attempting to characterize and predict aerodynamic loads [8]. Specifically, strong non-linear effects emerge under realistic conditions, i.e., for highly-separated, unsteady flows at high Reynolds numbers, contributing to the challenge in the load-estimation process. In order to mimic such realistic conditions by exploiting only a sparse set of sensors, existing data-driven methods are continuously improved while novel approaches are proposed. Among other techniques, complex networks have been used to reconstruct the time-series characterization of a complex system [9]. Specifically, complex networks have recently emerged as a versatile and powerful tool to study fluid flows [10], including vortical flows [11, 12], turbulent-combustor dynamics [13–15], as well as mixing in wall-bounded turbulence [16, 17]. More in detail, transition networks (thanks to their connection with Markov models [9]) have been successfully employed for time series reconstruction [18–21], as well as for reduced-order modeling [22, 23] and control [24].

In the current study, we exploit transition networks to perform signal estimation from highly-separated experimental flows when sparse sensors are available (FIG.1). The main objective is to propose and test a methodology capable of exploiting sparse and noisy datasets under unsteady conditions for signal estimation, thus potentially avoiding the collection of large datasets typical of data-driven approaches. Although transition networks have already been used to generate time series from a training dataset, they have been mainly employed for signal reconstruction. Namely, in the reconstruction process, the newly-generated time series are only expected to be globally similar (i.e., sharing similar statistical features) to the reference time series included in the training dataset (see FIG. 2d, top panel). Instead, in the present work, we perform signal estimation in real-time, namely to generate new signals that, based on sparse input data, estimate the instantaneous aerodynamic state. Thereby, the new series' specific (statistical)

* g.iacobello@queensu.ca

† frieder.kaiser@queensu.ca

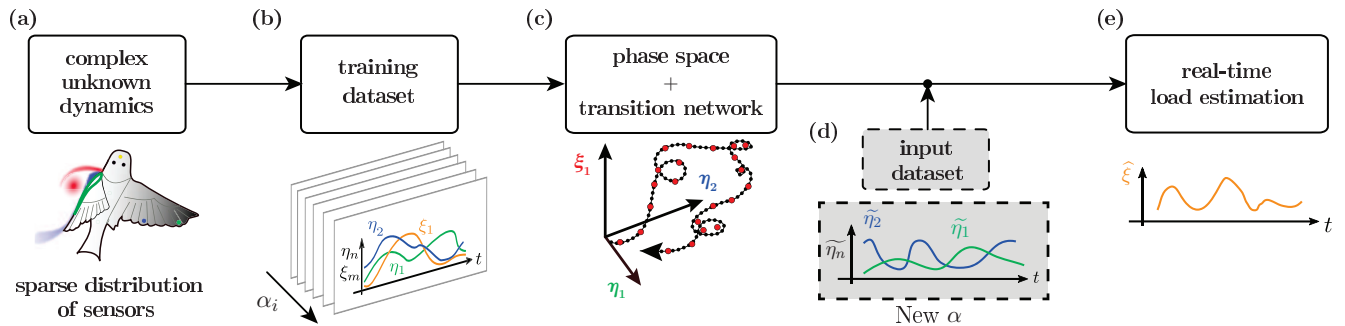


FIG. 1. Schematic of the workflow for the estimation process: (a) Complex (bio-inspired) dynamical system with sparse sensors; (b) Training dataset made up of a collection of time series for different configurations, α_i . Each collection comprises N time series, $\eta_n(t)$, from sparse sensors and M time series, ξ_m , corresponding to the variables to estimate; (c) Phase space definition of dimension equal to $N + M$, and construction of the transition networks; (d) Collection of a testing dataset of input time series, $\tilde{\eta}_n$; (e) Estimation of the M unknown signals, ξ_m , using the real-time input in panel (d) and a pre-trained transition networks of panel (c).

features can be different from those of the time series included in the training dataset (see FIG. 2d, bottom panel). As such, in contrast to other transition network-based approaches [e.g., 21, 23], we take into account the information coming from a testing dataset during the estimation process (FIG. 1d). Hence, the estimated load signal has to agree with the measured input data, making the signal estimation process significantly different than previously proposed reconstruction algorithms.

Two network-based strategies are proposed that allow for signal estimation, as described in sections II A and II B. The two strategies are tested on a simple yet challenging, experimental test case of an accelerated elliptical plate (section III), captured by only two differential pressure sensors. Results of the load estimates are presented in section IV, where we assess the capabilities and limitations of both network strategies to generate new signals in real-time in the presence of input data. Although this work represents a first attempt towards applying transition networks to realistic flows with sparse and noisy datasets, we show that transition networks can represent a valid alternative to other data-driven methods. Conclusions and future outlook are eventually drawn in section V.

II. TRANSITION NETWORKS WITH REAL-TIME INPUT

This section describes the signal estimation process, which exploits the features of a transition network built on an experimental training dataset, and a testing dataset of sparse pressure measurements enforcing a constraint to the estimation process of unknown load signals. As shown in FIG. 1, the overall method is characterized by four main steps: (i) the collection of a training dataset (FIG. 1b); (ii) the definition of a phase space from training data and the construction of transition networks (FIG. 1c); (iii) the measurement of (real-time) input data (FIG. 1d); (iv) the estimation of the load signal (FIG. 1e).

The training dataset consists of N synchronized time series from sparse sensors (here pressure probes) and M signals corresponding to the variables that have to be estimated (here load time series). In general, the training dataset can comprise multiple collections of $N + M$ sets of synchronized time series (see FIG. 1b), where each collection belongs to a different configuration parameter value, α_i . The configuration parameter can be, e.g., the Reynolds number, a boundary condition, or a geometrical configuration. In this work, α represents different angles of attack (see section III).

An $(N + M)$ -dimensional phase space can then be obtained from the training dataset, where each of the $N + M$ variables corresponds to a direction, η_n or ξ_m , in the phase space with $n = 1, \dots, N$ and $m = 1, \dots, M$. In this study, we consider only 3D phase spaces with $N = 2$ pressure signals and $M = 1$ forces (see section III). The rationale behind the phase space construction is to provide a geometrical representation of a multivariate time series, where each set of values $\{\eta_1(t), \eta_2(t), \xi(t)\}$ at a given time, t , indicates a unique dynamical state of the (flow) system through a unique point in the phase space. By mapping signal data at different times into the phase space, an oriented trajectory can be formed whose direction is in increasing time. FIG. 2(a) shows a 3-D phase space with directions η_1 , η_2 and ξ , and an exemplifying trajectory depicted as a blue dotted arrow.

Trajectory points in the phase space are then grouped by means of a clustering algorithm. This operation is usually performed to gain a simplification of the trajectories in the phase space, thus providing a reduced-order representation of the system [23]. Although the algorithm's choice is generally problem-dependent, the underlying

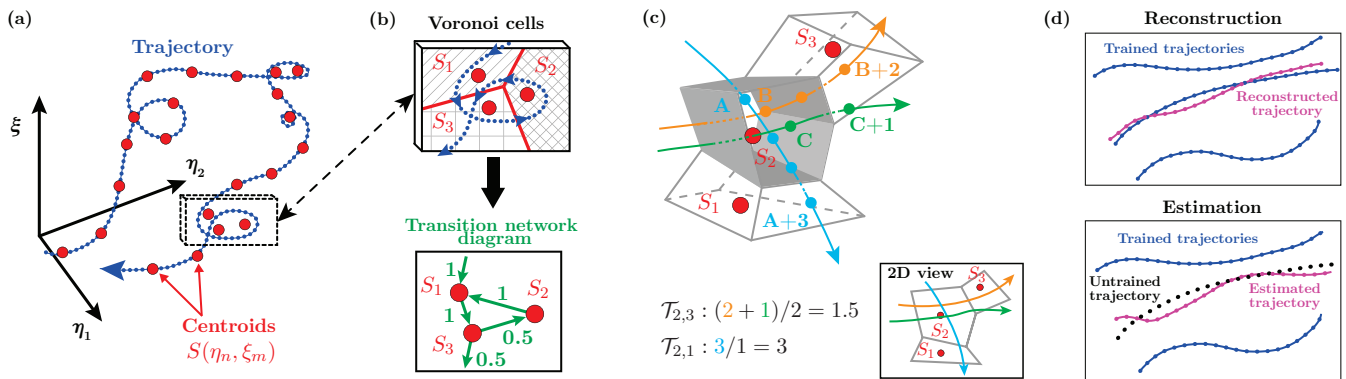


FIG. 2. (a) An example of 3D phase space with a trajectory (blue dotted line) and clusters centroids (red dots). (b) A zoomed inset in the trajectory, displaying three different Voronoi cells associated to three centroids. The transition network diagram refers to the inset, where green arrows indicate the direction of transition while numbers refer to transition probability values. (c) Schematic for the computation of transition times. The Voronoi cell referred to S_2 is highlighted through gray faces, while the remaining two cells for nodes S_1 and S_3 are highlight via gray edges. (d) Sketch illustrating the difference between reconstruction (top) and estimation process (bottom) of a trajectory in a 2D phase space.

rationale is to rely on a spatial-proximity algorithm since nearby points in the phase space refer to a similar dynamical state. Following Fernex *et al.* [21] and Li *et al.* [23], the k -means algorithm, in conjunction with the k -means++ improvement [25], is employed in this work to cluster trajectory points in the phase space, being a simple yet widely used technique to extract coherent clusters in an unsupervised manner [25, 26].

The k -means algorithm partitions the phase space into Voronoi cells represented by their cell centroids, S^α , whose entries are the centroid's coordinates in the phase space. The superscript \bullet^α here indicates that the clustering is applied to the trajectory corresponding to the configuration α of the training dataset. In FIG. 2(a), cluster centroids are depicted as red dots, capturing the essential features of the blue-dotted trajectory. The inset in FIG. 2(b) presents three Voronoi cells associated with three centroids, where red straight lines indicate the cell edges. Note that, although the k -means performs an unsupervised clustering, it requires an *a priori* definition of the number of clusters (i.e., centroids), N_{cl} , which should be large enough to capture the essential geometrical features of the phase space trajectories. After N_{cl} is fixed, the k -means algorithm is applied to each collection of time series, where each collection corresponds to a configuration parameter value, α_i .

Transition networks are eventually constructed from clustered trajectories, where cluster centroids are assigned to network nodes. Accordingly, a univocal correspondence exists between Voronoi cells, their centroids, and network nodes, all indicated through the symbol S . Network links are weighed on the probability of (temporal) transition between two nodes. In particular, the transition probability between two nodes, S_i^α and S_j^α is defined as

$$\mathcal{P}_{i,j}^\alpha = \frac{N(S_i^\alpha, S_j^\alpha)}{N_{all}(S_i^\alpha)}, \quad i, j = 1, \dots, N_{cl}, \quad (1)$$

where $N(S_i^\alpha, S_j^\alpha)$ is the number of times that trajectories directly transit from node S_i^α to node S_j^α , while $N_{all}(S_i^\alpha)$ is the total number of times that trajectories exit from node S_i^α . In general, $\mathcal{P}_{i,j}$ is not symmetric, i.e., $\mathcal{P}_{i,j} \neq \mathcal{P}_{j,i} \forall i \neq j$, so that the network is directed and links can be illustrated by means of arrows indicating the direction of transition [27]. For example, the blue trajectory in the inset of FIG. 2(b) uniquely transits from S_1 to S_3 , such that $\mathcal{P}_{1,3} = 1$, as reported in the transition network diagram where links are depicted as green arrows. Moreover, $\sum_{j=1}^{N_{cl}} \mathcal{P}_{i,j} = 1$, and $\mathcal{P}_{i,i} = 0$ (by definition of direct transition between nodes [23]) for any $i = 1, \dots, N_{cl}$.

To fully characterize the transition properties of the network, transition times, $\mathcal{T}_{i,j}^\alpha$, are also defined as the average amount of time needed for the transition from a node S_i^α to a node S_j^α [23]. FIG. 2(c) shows a 3-D sketch to illustrate the computation of transition times for a given reference cell identified by S_2 , where three trajectories (or three intervals of the same trajectory) are illustrated as colored dotted arrows. The orange trajectory enters the cell of S_2 on point B and exits on point $B+2$ so its transit time is equal to 2, while the transit times for cyan and green trajectories are equal to 3 and 1, respectively. The transition times are then computed as the average transit times between nodes; e.g., $\mathcal{T}_{2,3} = 1.5$ in FIG. 2(c) since the overall transit time is equal to 3, and there are two trajectories (the orange and green ones) transiting from S_1 to S_3 . As per matrix \mathcal{P} , the transition times matrix, \mathcal{T} , is also generally asymmetric ($\mathcal{T}_{i,j}^\alpha \neq \mathcal{T}_{j,i}^\alpha$).

At this stage, the procedure exploits the features of the transition-probability matrix, \mathcal{P} , and the transition-time

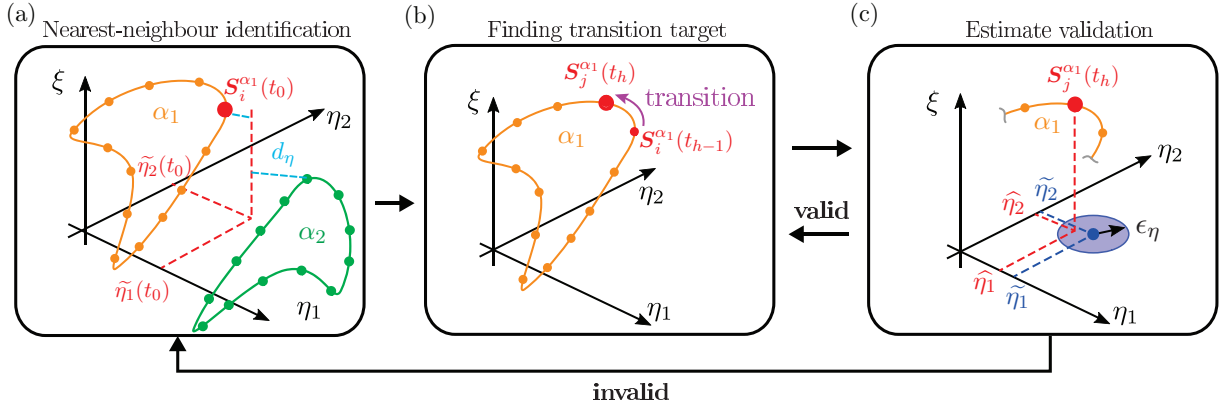


FIG. 3. Schematic of the NNV method for a 3D phase space, including two trained trajectories depicted as orange and green dotted lines. (a) Initial estimate of the force, $\xi(t_0)$, based on nearest-neighbors of initial pressure measurements. (b) Estimation using target nodes from the transition network. (c) Validation of the predicted load with input pressure data, $\hat{\eta}_1, \hat{\eta}_2$.

matrix, \mathcal{T} , to generate a new set of signals (FIG.1e). Although typical approaches perform a signal *reconstruction* (FIG. 2d, top) by means of a random walk into the transition network [18, 19, 21], several other strategies could be adopted owing to the versatility in the transition network construction. Here we present two strategies to perform signal *estimation*: transition network with nearest-neighbor validation (NNV); and weighted-average-based (WAB) transition network. The difference between reconstruction and estimation is shown in the schematic of FIG.2(d). Signal reconstruction aims to generate a new time series with (statistical) features similar to a trajectory belonging to the training dataset (blue trajectories in FIG.2d). In contrast, signal estimation aims to generate a new time series whose features were not included in the training dataset (green trajectory in FIG.2d). The latter approach represents a more challenging operation for data-driven methods, which instead usually rely on a very-large training dataset to provide the best possible outcome.

Additionally, in both strategies proposed here, we assume that input values from N time-series are known during the signal generation. For example, input values can originate from a set of N sparse pressure sensors collecting data in real-time, thereby supporting the time-series estimation (FIG.1d). The time series from the testing dataset are hereafter indicated via $\hat{\bullet}$ notation, namely $\{\hat{\eta}_1, \hat{\eta}_2, \hat{\xi}\}$; note that only η_1 and η_2 variables (i.e., the sparse pressure measurements) are considered as input data, while ξ (i.e., the force signal that has to be estimated) is only used as a reference signal to assess the estimation performance. Including the testing dataset in the estimation process implies that the construction of the new signal has to account for $\{\hat{\eta}_1, \hat{\eta}_2\}$ values. This procedure is in contrast to previous approaches – mainly performing signal reconstruction – where the newly-generated time series are only expected to be globally similar (i.e., sharing similar statistical features) to the reference time series rather than locally (i.e., at each time step). In order to distinguish from signals in the training and testing datasets, the newly generated signals are hereafter indicated via $\hat{\bullet}$ notation, namely $\{\hat{\eta}_1, \hat{\eta}_2, \hat{\xi}\}$. Finally, we note that an estimated time-vector, \hat{t} , can also be defined since, in general, \mathcal{T} entries do not exactly correspond to the time step Δt (a consequence of the clustering operation).

A. Transition networks with nearest-neighbor validation (NNV)

The NNV approach applies the idea classic idea of Markov chains modeling (typically used for signal reconstruction) where, starting from a node in the network, a path is obtained by *walking* through the network following the transition probabilities of each link. The NNV extends the classic approach to take into account the input (testing) data, $\{\hat{\eta}_1(t), \hat{\eta}_2(t)\}$, coming from sparse pressure sensors. It consists of the following three main procedural steps (see FIG. 3(a-c)), which can be defined as follows:

1. At the first time instance, t_0 , a nearest-neighbor criterion is adopted to estimate $\hat{\xi}$ (as shown in FIG. 3a) because a transition approach requires at least two times. The node, $S_i^\alpha(t_0)$, with the shortest Euclidean distance, $d_\eta = \|\hat{\boldsymbol{\eta}}(t_0) - \boldsymbol{\eta}_i\|_2$, with respect to the measured pressures, $\hat{\boldsymbol{\eta}}(t_0) = \{\hat{\eta}_1(t_0), \hat{\eta}_2(t_0)\}$, is then identified as the most reliable for the estimation of the force at t_0 . Note that $S_i^\alpha(t_0)$ is searched among all trajectories for all α . For example, in FIG. 3(a), $S_i^\alpha(t_0)$ is found for the trajectory corresponding to α_1 . Accordingly, the force

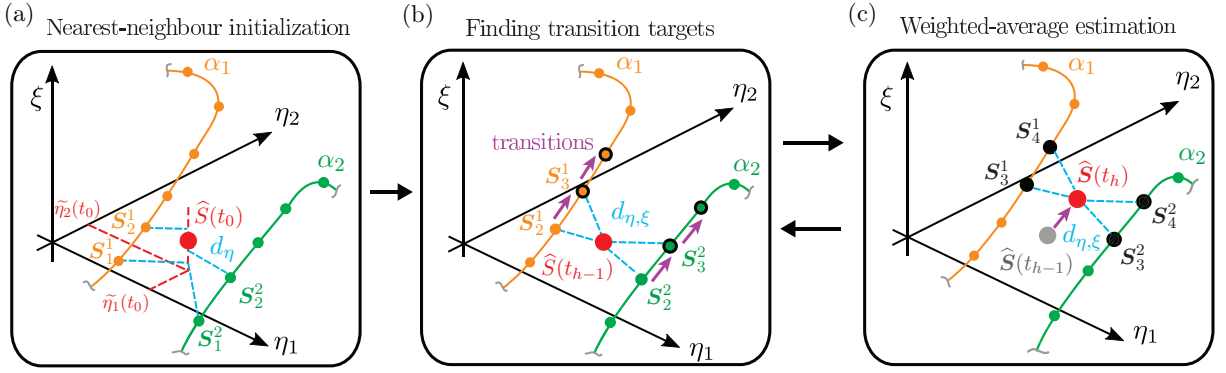


FIG. 4. Schematic of the WAB method for a 3D phase space, including the same two trained trajectories shown in FIG. 3. (a) Initial estimate of the load by weighted-average using the 2D distance d_η . (b) Identification of transition targets. (c) New estimation using transition targets (highlighted in black) for the weighted-average.

signal is estimated as $\widehat{\xi}(t_0) = \xi(\mathbf{S}_i^\alpha(t_0))$, where this notation indicates that $\widehat{\xi}(t_0)$ is equal to the ξ coordinate of the node $\mathbf{S}_i^\alpha(t_0)$, while $\widehat{t}_0 = t_0$;

2. The node $\mathbf{S}_i^\alpha(t_{h-1})$ found at the (generic) previous time, t_{h-1} with $h \geq 1$, can then be exploited as a source node for a transition path in the network, so that the transition probabilities can be used to perform a transition-based estimation (FIG. 3b). A new target node, $\mathbf{S}_j^\alpha(t_h)$ (shown as a larger filled red circle in FIG. 3b), is found following the path of maximum probability, i.e. finding the node that maximizes the transition probability $\mathcal{P}_{i,j}^\alpha$, with $j = 1, \dots, N_{cl}$. The estimated force is then computed as $\widehat{\xi}(t_h) = \xi(\mathbf{S}_j^\alpha)$, while the estimated time is $\widehat{t}_h = \widehat{t}_{h-1} + \mathcal{T}_{i,j}^\alpha$. It is worth noting that the node \mathbf{S}_j^α is selected to satisfy the condition $\widehat{t}_h \geq t_h$ (in general, the time steps of the input dataset and the estimated signal might not be the exactly the same).
3. The third step of NNV consists of a validation of the target node by exploiting the input (testing) data. The validation is done by checking the condition

$$d_\eta = \|\widetilde{\boldsymbol{\eta}}(t_h) - \widehat{\boldsymbol{\eta}}(t_h)\|_2 < \epsilon_\eta, \quad (2)$$

where ϵ_η is a threshold value (associable to the noise level of the training data, see section IV). Here, d_η is the Euclidean distance between the input pressure values, $\widetilde{\boldsymbol{\eta}}(t_h) = \{\widetilde{\eta}_1(t_h), \widetilde{\eta}_2(t_h)\}$, and the values of the pressure corresponding to the current target node, $\widehat{\boldsymbol{\eta}}(t_h) = \{\widehat{\eta}_1(t_h), \widehat{\eta}_2(t_h)\}$. The transition-based estimation continues as long as $d_\eta < \epsilon_\eta$ is satisfied, whereas a new node is identified through the nearest-neighbor approach as in step (1).

The validation check on step 3 is mainly required because the transition path naturally tends to follow a given trajectory in the phase space for a specific α (e.g., see the orange trajectory in FIG. 3). Therefore, without the condition (2), the estimated force would tend to reconstruct one of the force time series included in the training dataset (i.e., the path remains permanently in the same trajectory, as shown in the top panel of FIG. 2d). Accordingly, the NNV is expected to work well only if the configuration that has to be estimated is very similar to one of the configurations included in the training dataset. This limitation of the NNV algorithm implies that a large training dataset is still required for a generic setup with different unsteady motions.

B. Weighted-average-based (WAB) transition networks

To overcome some of the limitations of the NNV, other strategies can be adopted for the estimation step. In particular, to avoid collecting a large training dataset, the transition features of more than one trajectory can be concurrently exploited to estimate the unknown force signal. The WAB method follows this idea by performing a weighted average among different states in the phase space to create a new trajectory of newly-generated nodes, $\widehat{\mathbf{S}}(t)$, and comprises the following three main steps (see FIG. 4):

1. At the first time, as for the first step of NNV, a 2D nearest-neighbor approach is used to calculate $\widehat{\xi}$. A set, \mathbf{S}_{nn}^α , of N_{nn} nodes is selected for each configuration α . Specifically, each set of nodes comprises the closest N_{nn} nodes

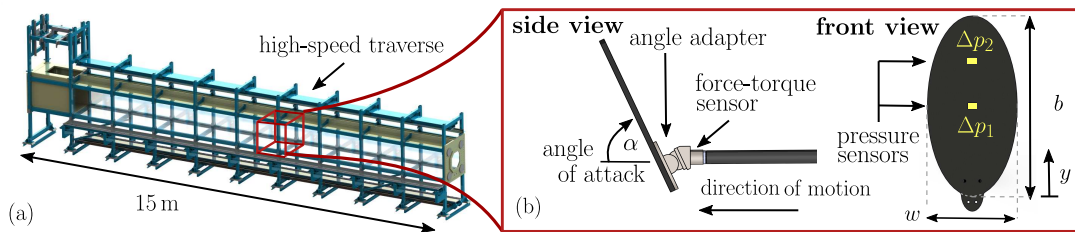


FIG. 5. (a) Towing-tank facility; (b) front and side view of the elliptical plate model with force-torque sensor, an angle adapter to determine α and two differential pressure sensors.

to the measured pressures of the testing dataset, namely $\{\tilde{\eta}_1(t_0), \tilde{\eta}_2(t_0)\}$. For example, in FIG. 4(a), $N_{nn} = 2$ and the closest nodes to the two configurations α_1 and α_2 are identified by dashed cyan lines, which highlight the 2D distances $d_\eta = \|\boldsymbol{\eta}(\tau_i^\alpha) - \tilde{\boldsymbol{\eta}}(t_0)\|_2$. The force value, $\hat{\xi}(t_0)$, is then evaluated as the weighted average of the ξ values of each node in \mathcal{S}_{nn}^α , namely

$$\hat{\xi}(t_0) = \frac{\sum_\alpha \sum_i w_i^\alpha \xi(\mathcal{S}_i^\alpha)}{\sum_\alpha \sum_i w_i^\alpha}, \quad (3)$$

where $\mathcal{S}_i^\alpha \in \mathcal{S}_{nn}^\alpha$, while $w_i^\alpha = 1/d_\eta$ are the distance-based weights. The new node $\hat{\mathcal{S}}(t_0) = \{\tilde{\eta}_1(t_0), \tilde{\eta}_2(t_0), \hat{\xi}(t_0)\}$ is then obtained, which is illustrated as a filled red dot in FIG. 4(a);

2. The transition probabilities of the networks are then used to continue estimating the force signal. At a generic time t_h , the N_{nn} closest nodes, \mathcal{S}_{nn}^α , are first identified for the previously estimated node $\hat{\mathcal{S}}(t_{h-1})$ (see filled red circle in FIG. 4b). In particular, the nodes in \mathcal{S}_{nn}^α are selected to minimize the Euclidean distance, $d_{\eta,\xi}$, between $\hat{\mathcal{S}}(t_{h-1})$ and the nodes belonging to each trajectory. We note that, differently from the previous procedural step where d_η was used, here $d_{\eta,\xi}$ represents a 3D distance, as shown by cyan dashed lines in FIG. 4(b). For any node in \mathcal{S}_{nn}^α , the transition matrix is exploited to identify the transition target nodes following the criterion of maximum transition probability. Target nodes are highlighted by black circles in each trajectory of FIG. 4(b), while transitions are shown via purple arrows;
3. A weighted average of the ξ values of the target nodes is eventually computed to estimate the force value $\hat{\xi}$ at time t_h , thus obtaining the point $\hat{\mathcal{S}}(t_h)$. Equation (3) is still exploited, where the weights w_i^α are here defined as $w_i^\alpha = 1/d_{\eta,\xi}$, with $d_{\eta,\xi}$ equal to the previously-computed 3D distance between the reference node and source nodes (cyan dashed lines in FIG. 4b-c). The estimated time \hat{t}_h is also computed as the sum of the previous estimated time, \hat{t}_{h-1} , and a weighted-average transition time from equation (3) where transition times \mathcal{T} are used instead of ξ .

A procedure similar to WAB can be found in Appendix F of Fernex *et al.* [21]. However, in that work, the weighted average is evaluated between two configurations identified *a priori*. In this work, instead, any configuration α of the training dataset is taken into account, since, in general, one does not know *a priori* the α value for the present estimation. Consequently, one does not know *a priori* the best two (or more) configurations to perform the weighted average. Moreover, we emphasize that the estimation process has to account for the measured pressures of the testing dataset.

Finally, it should be noted that a 3D distance is used instead of a 2D distance in step 3 to provide more robustness against ambiguous estimations. These arise when the η_1 and η_2 values of the nodes, τ_i^α , are similar, but their ξ values are significantly different.

III. EXPERIMENTAL TEST CASE

As a test case for the transition-network frameworks presented in section II, realistic experimental flow data were captured in a highly-separated and unsteady flow at a high Reynolds number. In particular, the canonical flow around an accelerating elliptical plate was characterized via pressure and load measurements, and the same experimental setup was used to obtain both training and testing datasets as described in section II.

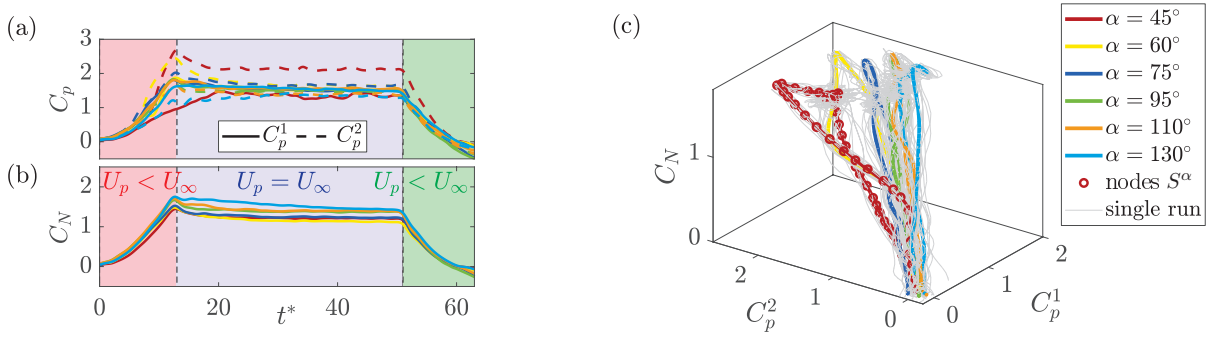


FIG. 6. Normalized plots of (a) the differential pressures, and (b) the plate-normal force as a function of the normalized time $t^* = U_\infty t / D_h$ and for various angles of attack. The acceleration stage (red), steady stage (blue), and the deceleration stage (green) are highlighted. (c) 3D phase space built on C_N , C_p^1 , and C_p^2 . Phase-averaged data (colored), and single-run data (gray) are both shown. For $\alpha = 45^\circ$ (red trajectory), $N_{cl} = 60$ nodes, S^α (corresponding to cluster centroids), are also displayed.

The experiments were performed in a fully-enclosed, water-filled (viscosity ν), 15 m long towing-tank facility with $1 \text{ m} \times 1 \text{ m}$ cross-section (FIG.5a). The model consisted of an elliptical plate (FIG.5a), with principal axes $b = 0.3 \text{ m}$ and $w = 0.15 \text{ m}$ and a cross-sectional area $A = \pi b w$. The model was connected to the traverse above the towing tank via a horizontal sting with diameter $0.08b$ and length $2b$, and a vertical symmetric profile of thickness $0.08b$. The plate was towed from rest with the plate velocity U_p accelerating at a rate of 0.4 m/s^2 until hitting its final velocity $U_\infty = 1 \text{ m/s}$, resulting in a terminal Reynolds number of $Re = U_\infty b / \nu = 194\,000$. The plate velocity ($U_p = U_\infty$) is then kept constant over a distance of $\sim 40D_h$ before it is decelerated to rest, where D_h is the hydraulic diameter. The same kinematics were tested for the plate being mounted at various angles of attack α (as defined in FIG.5b), in the range $45^\circ \leq \alpha \leq 135^\circ$.

Two Omega differential pressure transducers capture the instantaneous differential pressure Δp between the two sides of the plate. FIG.5(b) shows the positions of the two pressure transducers at $y/b = 0.5$ (Δp_1) and $y/b = 0.75$ (Δp_2), respectively. The pressure sensors measure a range of $\pm 6895 \text{ Pa}$, and have a response time of 10^{-3} s , and an accuracy of $\pm 0.25\%$ of the full-scale best fit straight line (FS BFSL) with hysteresis and repeatability of 0.2% FS. In order to measure forces and moments on the plate, an ATI six-axis force-torque sensor is mounted between the plate and the horizontal sting. The transducer has a resolution of 0.125 N . Pressures and forces were recorded at a sampling frequency of 1000 Hz .

FIG.6(a-b) presents the temporal evolution of the normalized pressures $C_p^i = 2\Delta p_i / \rho U_\infty^2$, and the plate-normal load $C_N = 2F_N / \rho A U_\infty^2$, for the six angles of attack. Here $i = 1, 2$ refers to sensor position at $y/b = 0.5$ and $y/b = 0.75$, respectively. The pressures and loads were phase-averaged over 10 runs, and temporally filtered with a least-squares estimator [28]. The standard deviation of the run-to-run pressures (averaged over all runs of all α) is $\Sigma_p = 0.05$, and is of particular interest with regard to the validation step of the NNV algorithm (see FIG.3c), since Σ_p provides the order of magnitude for the acceptable error radius ϵ_η .

FIG.6(c) visualizes the same data of FIG.6(a-b) in a 3D phase space, whose directions are $\eta_1 = C_p^1$, $\eta_2 = C_p^2$ and $\xi = C_N$. Single-run data are also illustrated in FIG.6(c) as gray trajectories, in addition to the phase-averaged data (colored). For smaller α values, the spacing between different trajectories is notably visible (e.g., the red and yellow trajectories in FIG.6(c)), while similar pressures are observed for $\alpha > 75^\circ$, making it difficult in this phase space to distinguish between the trajectories of different α . As such, the present dataset is particularly challenging with regard to accurate load estimates using transition networks. Specifically, ambiguous states are likely to appear, namely points in the phase space with similar pressure values but different loads.

IV. RESULTS AND DISCUSSION

In this section we present the results of the application of the transition network strategies proposed in sections II A and II B to the experimental data described in section III. In particular, we explore the performance of the two strategies when the transition networks are used to estimate loads for omitted flow configurations, i.e., time series corresponding to α values that were not available in the training data. The angles of attack considered in the present analysis are $\alpha = \{45^\circ, 60^\circ, 75^\circ, 95^\circ, 110^\circ, 135^\circ\}$. Moreover, to mimic realistic estimation conditions, a randomly selected single-run (gray lines in FIG.6c) is used as testing time series, rather than the phase-averaged signals (colored trajectories in FIG.6c). In this way, we account for single-run noise, as phase-averaged signals are less noisy.

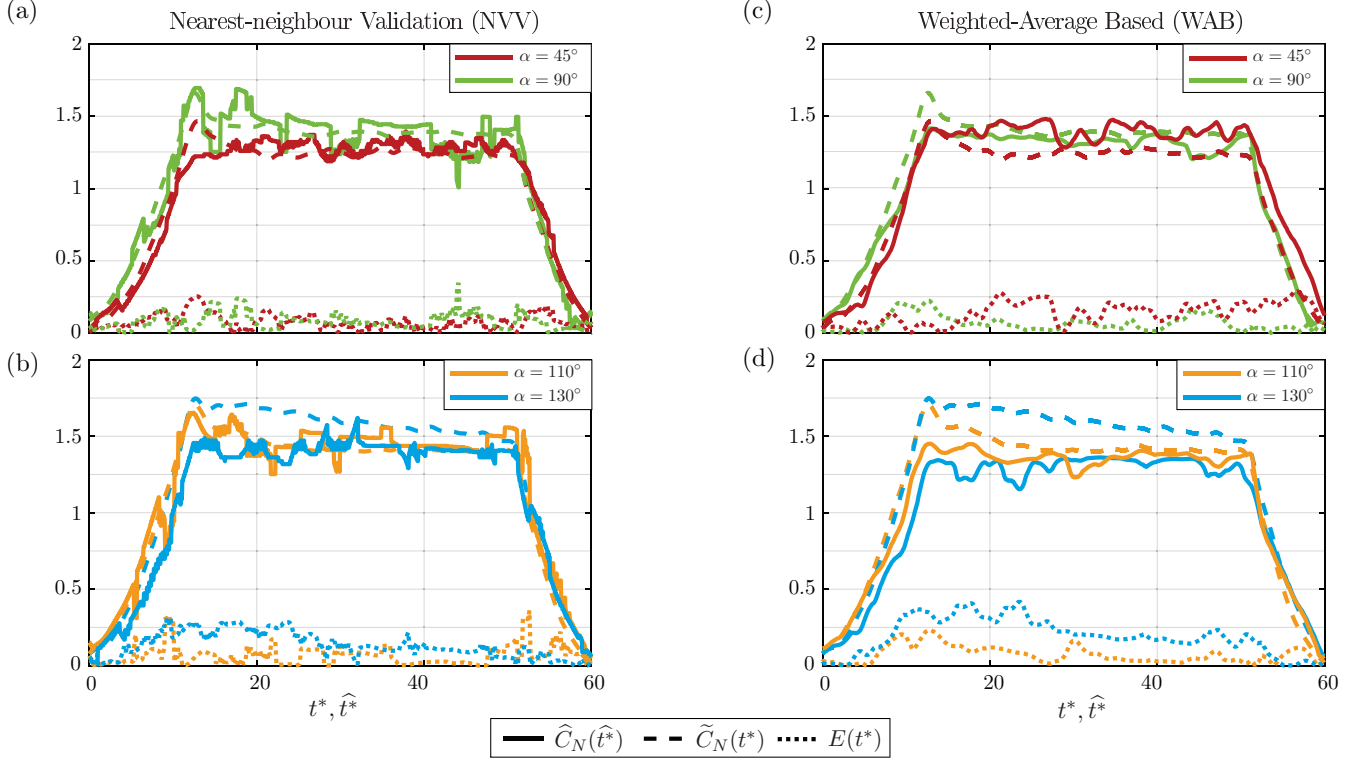


FIG. 7. Load estimates for various omitted α values. The input pressure data were randomly selected among all single runs of the respective α . Estimated loads \hat{C}_N (solid lines) and error E (dotted lines) are shown for (a,b) the NNV method and (c,d) the WAB method (E is evaluated using the \hat{t} closest to each t^*). The dashed lines refer to the measured load, \tilde{C}_N , as reference.

In the first step, transition networks are built using a training dataset made up of the pressure data ($\eta_1 = C_p^1, \eta_2 = C_p^2$) and the plate-normal load ($\xi = C_N$), as well as following the description provided in section II. The order of the experimental data is then reduced by clustering the phase space trajectories for each α into $N_{cl} = 300$ centroids, \mathbf{S}^α . By doing so, clustering is intended to reduce the number of trajectory points (temporal information) while preserving the identity of each trajectory corresponding to different α in the phase space. Centroids are shown in FIG.6(c) for the (phase-averaged) trajectory corresponding to the configuration $\alpha = 45^\circ$. In general, small values of N_{cl} serve to reduce the computational effort of the method. However, if N_{cl} is too small, the dynamics of a trajectory in the phase space cannot be properly resolved. In the present study, $N_{cl} = 300$ (with 12300 time-series instants, i.e., trajectory points) provides a good balance between estimation accuracy of the load \hat{C}_N and computational effort. A parametric analysis on the effects of N_{cl} on the results is provided in Appendix A.

Once the transition networks are established, a real-time estimate of the plate-normal load $\hat{\xi} = \hat{C}_N$ can be obtained by utilizing the pressure sensors' (real-time) input $\{\tilde{\eta}_1, \tilde{\eta}_2\} = \{\tilde{C}_p^1, \tilde{C}_p^2\}$ in combination with the NNV and WAB algorithms. Specifically, for the NNV strategy (FIG.7a-b) the error radius is set to $\epsilon_\eta = 3\Sigma_p$. Assuming Gaussian noise, $\epsilon_\eta = 3\Sigma_p$ ensures that states are only declared invalid when they deviate further from the real-time input ($\tilde{C}_p^1, \tilde{C}_p^2$) as 99.7% of the measured data. On the other hand, for the WAB strategy, the parameter N_{nn} is here set equal to 10. Although N_{nn} is usually set to be equal to 3 or 4 [21], $N_{nn} = 10$ leads to smoother load estimates without substantial changes in the overall results. After setting these parameters, the capabilities, as well as the limitations of the two estimation strategies, can then be tested for single-run data of each omitted α .

FIG.7 shows the resulting load estimates \hat{C}_N (solid lines) compared to the measured loads \tilde{C}_N (dashed lines) for different omitted α values (reported in each panel's legend). FIG.7 also presents the normalized error, $E = E_{abs}/\langle \tilde{C}_N \rangle$, of the estimates \hat{C}_N with respect to the test data \tilde{C}_N , where $E_{abs} = |\hat{C}_N - \tilde{C}_N|$ is the absolute error while $\langle \bullet \rangle$ indicates the time average. In general, the magnitude of E remains relatively small (less than 20%) throughout the whole estimation process (see also FIG.9). Nevertheless, the accuracy of the estimate varies depending on the flow stage (acceleration, steady-state, deceleration; see FIG.6a-b), the estimation strategy (NNV, WAB), as well as on the omitted α .

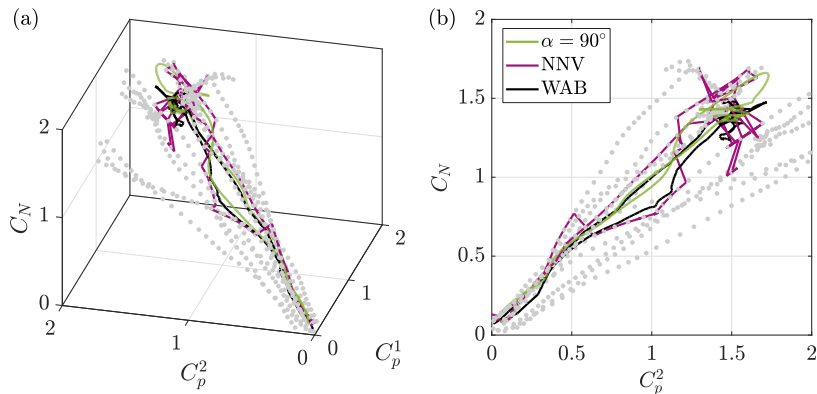


FIG. 8. Phase space trajectory of a randomly-selected single run at $\alpha = 90^\circ$ (green) compared to estimated trajectories in the phase space. The $\alpha = 90^\circ$ data was not included in the training data set. The unknown force \widehat{C}_N is estimated based on real-time input of \widetilde{C}_p^1 and \widetilde{C}_p^2 with the NNV (violet) and WAB (black) method, respectively. Subfigures (a,b) show different perspectives on the same visualization. Grey dots indicate the nodes from the transition networks.

While the NNV strategy can be expected to perform well when reconstructing a signal that is contained in the training data (FIG.2d), the limitations of the NNV algorithm become apparent when a non-trained signal has to be estimated. As shown in FIG.7(a-b), throughout the whole estimation process and for all omitted cases of α , a discontinuous load estimate is observed, with clear vertical jumps in \widehat{C}_N . This behavior is particularly evident for the $\alpha = 90^\circ$ case in FIG.7(a). Since the measured trajectory for a given α was omitted in the training data, as mentioned in section II A, the NNV approach tries to follow the trajectories from different configurations that instead are included in the training dataset. Hence, the NNV algorithm frequently detects invalid predictions, leading to a continuous re-initialization of the process (i.e., from the step 3 in FIG.3c to the step 1 in FIG.3a) and hence to a discontinuous load estimation.

FIG.7(c-d) presents load estimates obtained with the WAB approach for various omitted α . It is apparent that the WAB approach resolves the issue of discontinuous load estimates observed in the NNV approach. In fact, instead of jumping between different trained trajectories as per NNV, the WAB algorithm constructs a brand-new trajectory interpolating (through a distance-based weighted average) the data in the training dataset. To better emphasize the differences between NNV and WAB during the estimation process, in FIG.8 we illustrate the result of the estimation of the trajectory for $\alpha = 90^\circ$ via two phase-space visualizations. For most of the trajectory, the measured data (green line) lies between the states of the various transition networks (gray dots). While the NNV approach (violet line) jumps in between the transition networks in the attempt to follow the pressure input, WAB (black) can mimic the expected trajectory reasonably well.

By further comparing the results from the two strategies, we observe some similarities between NNV and WAB. In fact, the performance of both strategies tends to deteriorate if $\alpha = 130^\circ$ is omitted in the training dataset and then estimated (blue lines in FIG.7b,d). This behavior is due to the fact that the trajectory for $\alpha = 130^\circ$ is not fully surrounded by other trajectories in the phase space (see FIG.6c), but it is only close to the trajectory for $\alpha = 110^\circ$ (orange line in FIG.6c). From the point of view of NNV, this means that the algorithm will try to replicate the closest trajectory in the phase space (that is for $\alpha = 110^\circ$), and this can be clearly observed in the results of FIG.7(b). From the point of view of WAB, the weighted average to estimate the load for $\alpha = 130^\circ$ is performed using load data that are always lower than the expected \widehat{C}_N , so that the average is driven by lower C_N thus leading to higher errors. A different behavior can instead be observed in the estimation process for $\alpha = 90^\circ$ (green lines in FIG.7a,c), where the E values are generally smaller. In fact, as presented in FIG.8, the trajectory of $\alpha = 90^\circ$ is surrounded by states of various α . Consequently, the NNV can switch between several trained trajectories, while the weighted average in the WAB strategy can better interpolate to the estimated force.

V. CONCLUSIONS AND OUTLOOK

In this work, we extend the application of transition networks from signal reconstruction to load estimation with real-time input. In particular, we generate new signals that were not included in the training dataset, utilizing the input of N sparse sensors. Two network-based strategies are suggested and tested under realistic conditions of unsteady flows. In particular, the network-based approaches are tested over an experimental dataset of pressure and

force from an accelerating elliptical plate at various angles of attack. The two network strategies exploit the features of transition networks (which comprise the definition of a phase space and a clustering algorithm) and a real-time input of sparse pressure signals. The potential and limitations of the two strategies are discussed for estimates corresponding to different (omitted) angles of attack. The results indicate that transition networks can estimate configurations that were unknown during the training stage, with global estimation errors below 20%, and for some cases below 10%.

While the current strategies represent a first effort to employ transition networks to estimate aerodynamic loads in unsteady and high-Reynolds number flows, several methodological advancements can be implemented to enhance the capabilities of the network-based approach. Transition networks do not represent a *black box* tool between input and output variables but provide a versatile framework that can be easily modified to account for advanced information on the flow system. For instance, additional physical insights can be included in the network model by expanding the size of the phase space, where additional axes could represent other measured variables of the system. In this regard, future efforts aim to incorporate external flow measurements (e.g., velocity or vorticity fields) in the transition network model, which can also rely on random walks with or without memory [21]. On this note, the outcomes from simple models could also be incorporated in the algorithms, either as additional axes of the phase space or as additional input data to constraint the process. With the aim to account for noise in experimental data, different clustering strategies could be applied (such as fuzzy algorithms), and the probabilistic nature of transition networks could be further exploited, e.g., implementing Bayesian statistics. Furthermore, different interpolating schemes can be used in the WAB strategy, where the weighted average can be performed on a limited set of configurations chosen via an optimization routine.

In conclusion, transition networks show potential for real-time estimation of unknown variables, even under challenging flow conditions and sparse training datasets. Therefore, we believe the network-based methodology, owing to its versatility, can be a promising tool for the real-time estimation of realistic flows even when limited by sparse data.

ACKNOWLEDGMENTS

DER acknowledges support from the Air Force Office of Scientific Research (AFOSR) under Grant No. FA9550-20-1-0086, monitored by Dr. Gregg Abate.

Appendix A: Parametric analysis on number of network nodes

This Appendix describes the effects the N_{cl} parameter on the estimation performances of the transition network strategies. We recall that N_{cl} indicates the number of nodes in the network, which correspond to the centroids of the Voronoi cells obtained from the k -means clustering.

FIG.9 shows the average performance of the two proposed network strategies when the number of centroids, N_{cl} , is varied. Here a global error is computed as $\langle E \rangle = \langle E_{abs} \rangle / \langle \tilde{C}_N \rangle$. For NNV (FIG.9a), the error is independent on N_{cl} , and the method works fairly well except for $\alpha = 130^\circ$, as discussed in section IV. In contrast, for WAB (FIG.9b), $\langle E \rangle$ increases for small N_{cl} values as it becomes comparable with the number of nodes used to perform the weighted average, $N_{nn} = 10$. As discussed in section IV, the WAB method performs well when intermediate configurations have to be estimated, which is confirmed in FIG.9(b) for $\alpha = \{75^\circ, 95^\circ, 110^\circ\}$. For both methods, $\langle E \rangle$ values for $N_{cl} = 300$ are below 10% for the intermediate case and below 20% for external cases in WAB, thus justifying the choice of $N_{cl} = 300$ in section IV.

-
- [1] J. Liao, D. Beal, G. Lauder, and M. Triantafyllou, Fish exploiting vortices decrease muscle activity, *Science* **302**, 1566 (2003).
 - [2] S. Portugal, T. Hubel, J. Fritz, S. Heese, D. Trobe, B. Voelkl, S. Hailes, A. M. Wilson, and J. R. Usherwood, Upwash exploitation and downwash avoidance by flap phasing in ibis formation flight, *Nature* **505**, 399 (2014).
 - [3] R. Zbikowski, Sensor-rich feedback control: a new paradigm for flight control inspired by insect agility, *IEEE Instru. Meas. Mag.* **7**, 19 (2004).
 - [4] S. Sterbing-D'Angelo, M. Chadha, C. Chiu, B. Falk, W. Xian, J. Barcelo, J. M. Zook, and C. F. Moss, Bat wing sensors support flight control, *PNAS USA* **108**, 11291 (2011).
 - [5] M. Le Provost, X. He, and D. R. Williams, Real-time roll and pitching moment identification with distributed surface pressure sensors on a ucas wing, in *2018 AIAA Aerospace Sciences Meeting* (2018) p. 0326.
 - [6] K. T. Wood, S. Araujo-Estrada, T. Richardson, and S. Windsor, Distributed pressure sensing-based flight control for small fixed-wing unmanned aerial systems, *Journal of Aircraft* **56**, 1951 (2019).

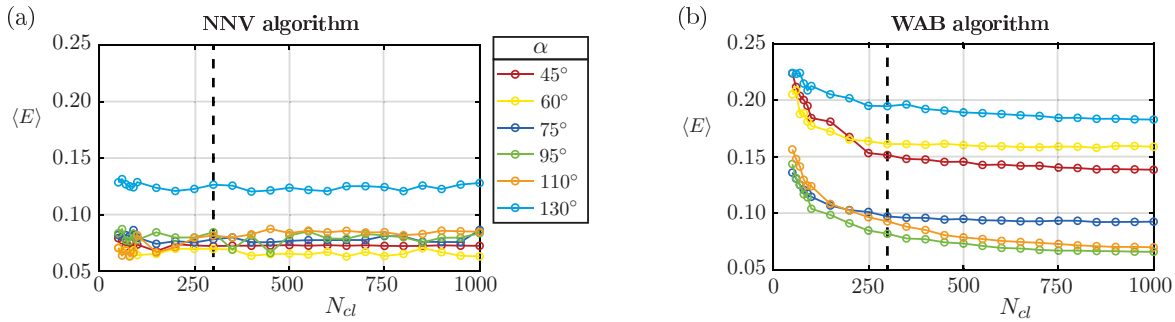


FIG. 9. Effect on the number nodes (i.e., cluster centroids) on the estimation performance. The legend indicates the estimated case. The dashed vertical line corresponds to $N_{cl} = 300$ as in section IV.

- [7] W. Hou, D. Darakananda, and J. Eldredge, Machine-learning-based detection of aerodynamic disturbances using surface pressure measurements, *AIAA J.* **57**, 5079 (2019).
- [8] L. Burelle, W. Yang, F. Kaiser, and D. E. Rival, Exploring the signature of distributed pressure measurements on non-slender delta wings during axial and vertical gusts, *Phys. Fluids* **32** (2020).
- [9] Y. Zou, R. Donner, N. Marwan, J. Donges, and J. Kurths, Complex network approaches to nonlinear time series analysis, *Phys. Rep.* **787**, 1 (2019).
- [10] G. Iacobello, L. Ridolfi, and S. Scarsoglio, A review on turbulent and vortical flow analyses via complex networks, *Physica A*, 125476 (2020).
- [11] K. Taira, A. Nair, and S. Brunton, Network structure of two-dimensional decaying isotropic turbulence, *J. Fluid Mech.* **795** (2016).
- [12] M. Gopalakrishnan Meena and K. Taira, Identifying vortical network connectors for turbulent flow modification, *J. Fluid Mech.* **915**, A10 (2021).
- [13] A. Krishnan, R. Sujith, N. Marwan, and J. Kurths, Suppression of thermoacoustic instability by targeting the hubs of the turbulent networks in a bluff body stabilized combustor, *J. Fluid Mech.* **916**, A20 (2021).
- [14] T. Kobayashi, S. Murayama, T. Hachijo, and H. Gotoda, Early detection of thermoacoustic combustion instability using a methodology combining complex networks and machine learning, *Physical Review Applied* **11**, 064034 (2019).
- [15] M. Murugesan and R. Sujith, Combustion noise is scale-free: transition from scale-free to order at the onset of thermoacoustic instability, *J. Fluid Mech.* **772**, 225 (2015).
- [16] G. Iacobello, S. Scarsoglio, J. Kuerten, and L. Ridolfi, Lagrangian network analysis of turbulent mixing, *J. Fluid Mech.* **865**, 546 (2019).
- [17] D. Perrone, J. Kuerten, L. Ridolfi, and S. Scarsoglio, Wall-induced anisotropy effects on turbulent mixing in channel flow: A network-based analysis, *Physical Review E* **102**, 043109 (2020).
- [18] A. Shirazi, G. Jafari, J. Davoudi, J. Peinke, M. Tabar, and M. Sahimi, Mapping stochastic processes onto complex networks, *J. Stat. Mech.* **2009**, P07046 (2009).
- [19] A. Campanharo, M. I. Sirer, R. D. Malmgren, F. M. Ramos, and L. Amaral, Duality between time series and networks, *PloS one* **6**, e23378 (2011).
- [20] M. McCullough, K. Sakellariou, T. Stemler, and M. Small, Regenerating time series from ordinal networks, *Chaos* **27**, 035814 (2017).
- [21] D. Fernex, B. R. Noack, and R. Semaan, Cluster-based network modeling—automated robust modeling of complex dynamical systems, arXiv preprint:2010.16364 (2020).
- [22] E. Kaiser, B. Noack, L. Cordier, A. Spohn, M. Segond, M. Abel, G. Daviller, J. Östh, S. Krajnović, and R. Niven, Cluster-based reduced-order modelling of a mixing layer, *J. Fluid Mech.* **754**, 365 (2014).
- [23] H. Li, D. Fernex, R. Semaan, J. Tan, M. Morzyński, and B. R. Noack, Cluster-based network model, *J. Fluid Mech.* **906** (2021).
- [24] A. Nair, C. Yeh, E. Kaiser, B. Noack, S. Brunton, and K. Taira, Cluster-based feedback control of turbulent post-stall separated flows, *J. Fluid Mech.* **875**, 345 (2019).
- [25] D. Arthur and S. Vassilvitskii, *k-means++: The advantages of careful seeding*, Tech. Rep. (Stanford, 2006).
- [26] S. Lloyd, Least squares quantization in pcm, *IEEE T. Inform. Theory* **28**, 129 (1982).
- [27] M. Newman, *Networks* (Oxford university press, 2018).
- [28] A. Savitzky and M. J. E. Golay, Smoothing and differentiation of data by simplified least squares procedures, *Anal. Chem.* **36**, 1627 (1964).